

ARTICLE

Solar-assisted co-electrolysis of glycerol and water for concurrent production of formic acid and hydrogen†

Received 00th January 20xx,
Accepted 00th January 20xx

Zunjian Ke,^{a,b} Nicholas Williams,^b Xingxu Yan,^c Sabrina Younan,^b Dong He,^a Xianyin Song,^e Xiaoqing Pan,^{c,d} Xiangheng Xiao*^a and Jing Gu*^b

DOI: 10.1039/x0xx00000x

Renewable electricity-driven water splitting provides a pathway to manufacturing hydrogen as a promising alternative to fossil fuels. A typical water electrolysis device is comprised of a cathodic hydrogen evolution reaction (HER) and an anodic oxygen evolution reaction (OER). Unfortunately, OER consumes most of the overall electricity supply while generating negligible economic value, which inhibits the large-scale deployment of the water electrolysis technology. Here, we explored alternatives to OER and demonstrated that electrooxidation of glycerol (a cheap byproduct of biodiesel and soap production) could lower anodic electricity consumption by up to 0.27 V while producing high-value formic acid with 96.2% Faradaic efficiency (FE). Further, glycerol electrooxidation was combined with photoelectrochemical HER to diminish the electricity requirement to 1.15 V, reducing ~30% electricity consumption relative to typical water electrolysis. More importantly, glycerol electrooxidation exhibits more economic profits due to the generation of high value-added formic acid. This study suggests that solar-assisted co-electrolysis of high-volume block chemicals and water may be an energy efficient and economically viable strategy to realize the sustainable production of value-added chemicals and hydrogen energy.

Introduction

The detrimental impact of global fossil fuel consumption on the climate and environment has instilled a tremendous interest in developing renewables-powered solutions to manufacturing clean energy.¹ As a crucial carbon-neutral energy carrier and chemical reaction intermediate, hydrogen has been recognized as a renewable alternative to fossil fuels.² At present, more than 100 Mt of hydrogen is manufactured per year. However, 95% is still produced by energy-extensive steam methane reformation, and only 4% through electricity-driven water splitting.^{3,4} Producing hydrogen by steam methane reformation renders the cost of hydrogen to be ~\$1.2–1.5/kg, whereas the cost of hydrogen produced via water electrolysis is more than \$4/kg. This high cost of hydrogen production substantially diminishes the market share for water electrolysis. Consequently, the cost of hydrogen production via water electrolysis must reduce to ~\$2/kg to achieve a large-scale application.^{5,6} Generally, costs

associated with water electrolysis are dictated by operation expenses and capital input, with the former primarily dominated by electricity consumption.⁴ Unfortunately, a high overall electricity input (>1.5 V of the cell voltage) is required for typical water electrolysis devices (Scheme 1a), which limits the industrial deployment of these devices.⁷ The culprit behind this barrier is the thermodynamically sluggish OER, which consumes the majority of electricity input while producing negligible economic benefits (~\$0.1/kg of oxygen price).⁸ As a consequence, exploring alternative strategies that circumvent sluggish OER thermodynamics while generating high-value products has the potential to lower energetic requirements and enable water electrolysis to replace traditional steam reforming processes. Recently, a few efforts have reported that employ lower-energetic anodic reactions (such as electrooxidation reactions of ethanol,⁹ urea,¹⁰ hydrazine,¹¹ and etc) in water electrolysis. While these explorations are interesting, the oxidation of the reported chemicals may not be sustainable. For instance, the electrooxidation of urea will contribute to the emission of carbon dioxide.

Herein, we investigate the electrooxidation of glycerol to formic acid as a promising substitute for OER. Theoretically, the redox potential of glycerol to formic acid is 0.69 V, 44% lower than the 1.23 V required for OER (Scheme 1a, b).¹² This indicates that utilizing glycerol electrooxidation as an anodic reaction could significantly lower electricity requirements. More importantly, glycerol is a cheap by-product of biodiesel and soap production (\$0.24/kg),¹³ whereas its major oxidation product, formic acid,

^a Department of Physics, Key Laboratory of Artificial Micro- and Nano-structures of Ministry of Education, Wuhan University, Wuhan 430072, Hubei, China. E-mail: xxh@whu.edu.cn

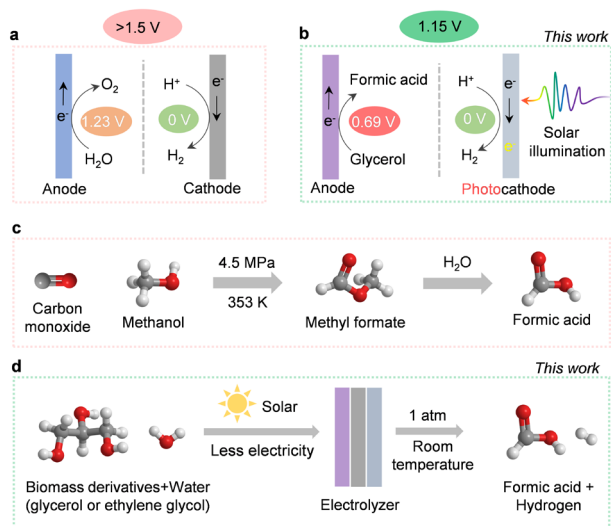
^b Department of Chemistry and Biochemistry, San Diego State University, San Diego, California 92182-1030, United States. E-mail: jgu@sdsu.edu

^c Department of Materials Science and Engineering, University of California, Irvine, Irvine, California 92697, United States.

^d Department of Physics and Astronomy, University of California, Irvine, Irvine, California 92697, United States.

^e College of Materials Science and Engineering, Hunan University, Changsha 410082, Hunan, China.

† Electronic Supplementary Information (ESI) available: [experimental section, supplementary SEM, XRD, TEM and XPS characterizations, and related electrochemical data]. See DOI: 10.1039/x0xx00000x



Scheme 1 Overview of hydrogen production and formic acid manufacturing. **a** Typical water electrolysis device. **b** Energy-efficient and value-added hydrogen production system in this work. **c** Industrial formic acid production. **d** Solar-assisted formic acid electro-synthesis in this work.

is widely used in fuel cell and hydrogen storage industries.¹⁴ As a high-value commodity chemical (\$1.0/kg),¹⁵⁻¹⁶ manufacturing formic acid by coupling glycerol electrooxidation with HER retains high economic value (\$17.25) upon producing 1 kg of hydrogen (Table S1, ESI[†]). In comparison, O₂ produced by traditional water electrolysis (Scheme 1a) is only worth \$0.80 to generate the same amount of hydrogen. In this regard, ambient glycerol electrooxidation will allow formic acid to be generated in a more sustainable manner than the industrial high temperature and pressure methyl formate hydrolysis (Scheme 1c).¹⁷ Therefore, highly efficient and selective electrocatalysts for glycerol oxidation are desired. However, most glycerol electro-oxidation catalysts so far are noble metals (like Pt¹⁸, Au¹⁹, Pd²⁰) and alloys (like PtRu²¹, PtSb²², Pd_xBi²³). Moreover, the reaction pathways of glycerol oxidation involve in various C₁ – C₃ intermediates which can interconvert into many different oxidation products, thus suffering from low selectivity.²⁴

In this work, we developed an efficient and cost-effective nitrogen-doped cobalt oxide (N-CoO_x) electrocatalyst. The catalyst is derived from an organometallic cobalt complex and can achieve a highly selective formic acid synthesis by glycerol electrooxidation (96.2% FE). The anodic electricity consumption reduced up to 0.27 V relative to OER, which is comparable with previous glycerol oxidation works.³²⁻³³ In order to further diminish the electricity requirements, a cathodic photoelectrochemical HER was coupled with anodic glycerol oxidation (Scheme 1b). The hybrid system could be driven by solar with an additional electricity supply of 1.15 V to accomplish concurrent production of formic acid and hydrogen. This value, to our understanding, is the lowest electricity input reported for water electrolysis (Table S2, ESI[†]). In addition, the versatility of the N-CoO_x catalyst was further confirmed by its ability to upgrade biomass-derived ethylene glycol into formic acid with a high FE of 62.3%. Overall, we have achieved highly selective, energy-efficient, and

economically viable co-production of hydrogen fuel and high-value chemicals by solar-assisted co-electrolysis of water and cheap biomass waste (Scheme 1d).

Results and Discussion

Material characterizations

The nitrogen doped cobalt oxide electrocatalyst (N-CoO_x) was directly deposited on carbon fibre paper by one-step facile atomic layer deposition (ALD). The precursor, a nitrogen-containing organometallic cobalt complex (Bis (N, N'-di-*i*-propylacetamidinato) cobalt (II)) (Fig. 1a, Fig. S1, ESI[†]), was employed as cobalt and nitrogen sources for in situ nitrogen doping (see ESI[†]). The morphology of N-CoO_x was characterized by scanning electron microscopy (SEM), in which the visibly smooth carbon surface confirms the uniform and ultrathin nature of the deposited catalyst film (Fig. S2a, ESI[†]). Atomic resolution high-angle annular dark-field (HAADF) scanning transmission electron microscopy (STEM) was employed to determine the structure and composition of N-CoO_x (Fig. 1b). The resulting images clearly show lattice fringes and three characteristic crystal facets with interplanar spacings equal to 0.286, 0.463, and 0.241 nm. These crystal facets were indexed to the (220), (111), and (311) planes of Co₃O₄ with a standard spinel structure, respectively. The corresponding fast Fourier transform (FFT) patterns (Fig. 1b, inset) suggest the presence of multiple crystalline orientations of N-CoO_x. Furthermore, the low magnification HAADF-STEM image and corresponding elemental mappings in Fig. 1c validate the uniform distribution of cobalt, oxygen, and nitrogen elements throughout the sample. These results are also confirmed by energy-dispersive X-ray spectroscopy of SEM (SEM-EDS) in Fig. S3, ESI[†]. The elemental compositions were further quantified by STEM-EDS (Fig. S4, ESI[†]), in which the presence of non-stoichiometric ratio of cobalt and oxygen suggests the existence of multiple types of cobalt oxides in N-CoO_x, corresponding effectively with FFT patterns in Fig. 1b. X-ray diffraction (XRD) patterns were collected to identify the crystal structure of the catalysts (Fig. S2b, ESI[†]).

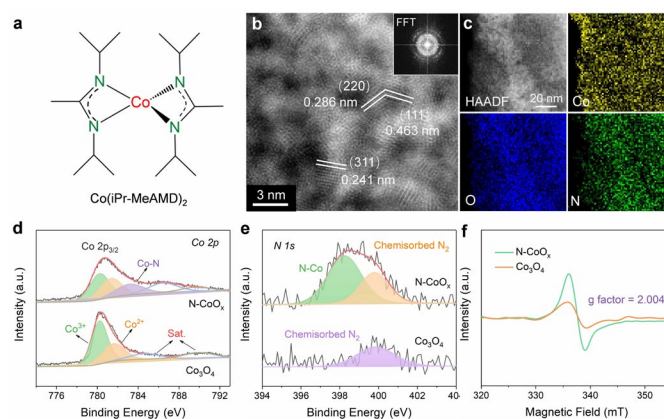


Fig. 1 Structure and chemical states of N-CoO_x. **a** Structure of Bis (N, N'-di-*i*-propylacetamidinato) cobalt (II) (Co(iPr-MeAMD)₂) complex for N-CoO_x synthesis. **b-c** HRTEM image and STEM-EDX elemental mapping of N-CoO_x (inset: fast fourier transform pattern). **d** XPS Co 2p, **e** XPS N 1s, and **f** EPR spectra of N-CoO_x and Co₃O₄.

In these results, only one broad peak, belonging to the amorphous substrate, was identified. Lack of distinct characteristic peaks in XRD pattern may be attributed to the catalyst's ultrathin nature.²⁵ On the other hand, the sample contains some amorphous regions in HAADF-STEM image (Fig. 1b), which is evidenced by the amorphous ring in FFT patterns (Fig. 1b), correlating well with the XRD results. The surface chemical states of N-CoO_x were elucidated by X-ray photoelectron spectroscopy (XPS) (Fig. 1d-e, Fig. S5, ESI[†]). XPS survey spectrum in Fig. S5, ESI[†] revealed the presence of Co and O elements in N-CoO_x and Co₃O₄ samples. Besides, an obvious N 1s signal at 399.1 eV in N-CoO_x inevitably confirmed the existence of N in N-CoO_x. In contrast, the N 1s signal in the Co₃O₄ control sample is negligible.²⁶ The peak at 398.2 eV in the fitted high-resolution N 1s spectra (Fig. 1e) for N-CoO_x references the existence of N-Co species, while the 399.9 eV peak identifies adsorbed N₂ on both N-CoO_x and Co₃O₄

samples.²⁶⁻²⁷ To analyse chemical states of cobalt, the Co 2p XPS spectra are provided in Fig. 1d. The Co 2p_{3/2} peaks for Co₃O₄ may be fitted to the peaks at 780.4 eV and 781.8 eV and are assigned to tetrahedral and octahedral Co-O coordination geometries, respectively.²⁸ Notably, the additional peak at 782.9 eV in Co 2p for N-CoO_x further confirmed the presence of Co-N bonds in the catalyst.^{26, 29} Here, it was worth noting that Co-Co interactions (around 778.8 eV) were not observed, precluding the presence of cobalt nitride species in N-CoO_x.³⁰ To further reveal the effects of N dopant, the defects of catalysts were characterized by electron paramagnetic resonance (EPR) spectroscopy (Fig. 1f). The strong EPR signal located at *g* = 2.004 corresponds to the existence of oxygen vacancies. In addition, N dopant's potential to induce additional oxygen vacancies is indicated by the N-CoO_x peak intensity being twice as that of Co₃O₄.^{26-27, 31}

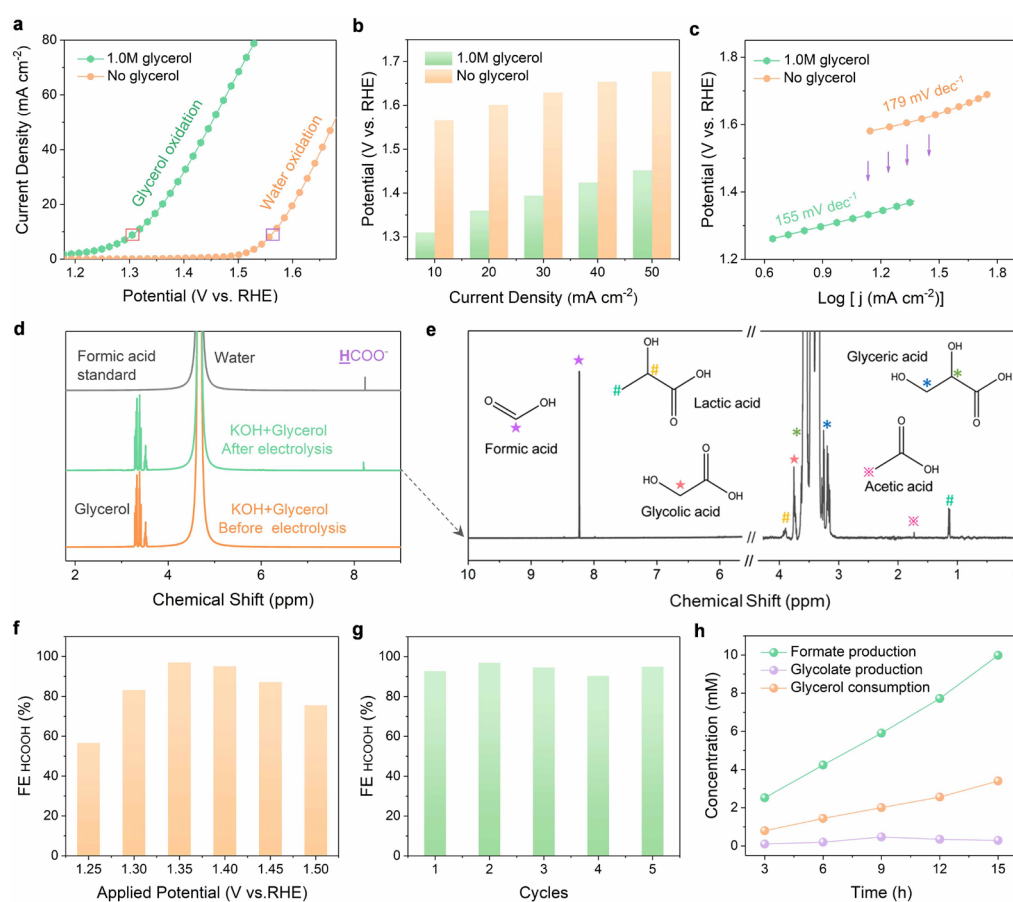


Fig. 2 Glycerol electrooxidation performance. **a** Linear sweep voltammetry (LSV) plots (all LSV plots were collected with a scan rate of 5 mV s⁻¹ in N₂-saturated electrolyte with no I-R compensation). **b** Input potentials at various current densities. **c** Tafel slopes for OER and glycerol oxidation in 1.0 M KOH solution both with and without 1.0 M glycerol. Purple arrows inset indicate the significant potential decrease at various current densities when 1.0 M glycerol is added. **d** ¹H NMR spectra of the formic acid standard and electrolytes (1.0 M KOH + 1.0 M glycerol) before and after 12 h of electrolysis at 1.35 V vs. RHE. Due to the higher initial glycerol concentration, the intensity of ¹H NMR peaks for glycerol did not decrease significantly after electrolysis. **e** High-resolution ¹H NMR spectra (water peak was removed from 4 to 6 ppm) of the 1.0 M KOH + 1.0 M glycerol solution after 12 h of electrolysis (the symbols on the top of the peaks represent each type of proton present). **f** Faradaic efficiencies of formic acid at various potentials (each potential underwent 12 h of electrolysis). **g** Faradaic efficiencies of formic acid for five successive electrolysis cycles at 1.35 V vs RHE. **h** Concentration changes of the reactant (glycerol), main product (formic acid), and representative intermediate species (glycolic acid) with electrolysis time.

Glycerol electrooxidation

Electrochemical investigations were conducted to compare the performance of N-CoO_x in glycerol oxidation to its performance in water oxidation. Compared to Co₃O₄, N-CoO_x required a lower potential (1.58 V) to reach the current density of 10 mA cm⁻² (Fig. S6a, ESI†). Likewise, higher activity of N-CoO_x was confirmed by its lower Tafel slope (179 mV dec⁻¹) with respect to Co₃O₄ (187 mV dec⁻¹) (Fig. S6b, ESI†). On average, the OER activities of both catalysts were very close and moderate, indicating that the N dopant did not contribute significantly to OER. Next, systematic elucidation of the electrocatalytic activity of N-CoO_x towards glycerol oxidation is provided in Fig. 2. Without glycerol, N-CoO_x showed moderate OER activity by delivering an onset potential of 1.50 V and a potential of 1.58 V at 10 mA cm⁻² (Fig. 2a). Addition of 1.0 M glycerol caused a negative shift in the onset potential and the potential at 10 mA cm⁻² to 1.2 V and 1.31 V, respectively. Here, a visibly significant shift of 0.3 V and 0.27 V occurred for the onset potential and the potential at 10 mA cm⁻², respectively. Upon evaluating the difference in potentials and current densities for N-CoO_x before and after adding glycerol, lower energetic requirements are witnessed for each current density when glycerol is present (Fig. 2b). This result verifies the aptitude of N-CoO_x for glycerol oxidation. It should be noted that the optimal glycerol concentration was determined to be 1.0 M by linear sweep voltammetry (LSV), where the lowest onset potential was determined by varying glycerol concentrations from 0 to 2.0 M. Notably, an extra peak at 1.45 V (pointed out by an arrow in Fig. S7, ESI†) appeared with the addition of 0.1 M glycerol, suggesting the ability of OER to compete with glycerol oxidation at a higher potential (>1.45 V) while using a lower concentration of glycerol.

The role of N dopant in enhancing kinetics for glycerol oxidation is demonstrated by the Tafel and impedance measurements. The Tafel slope (Fig. 2c) for glycerol oxidation was determined to be 155 mV dec⁻¹, which is lower than that of OER (179 mV dec⁻¹). This indicates that N-CoO_x achieves faster kinetics for glycerol oxidation relative to that of OER. To clarify the influence of N dopants on N-CoO_x catalytic activity, the oxidation performance of N-CoO_x and Co₃O₄ was compared (Fig. S8, ESI†). Results show that Co₃O₄ requires a higher potential (1.43 V) than N-CoO_x (1.31 V) to drive the current density of 10 mA cm⁻² for the reaction forward. Co₃O₄ also exhibited a higher Tafel slope (173 mV dec⁻¹) than N-CoO_x (155 mV dec⁻¹) (Fig. S8a, b, ESI†). Since Tafel slopes indicate the catalytic reaction rate's dependence on applied potentials, these results show that the N-CoO_x anode possesses much faster glycerol oxidation kinetics than that of Co₃O₄. This conclusion is further supported by the electrochemical impedance spectra (EIS), where N-CoO_x showed much lower electric impedance than Co₃O₄ (Figure S8c, Table S3, ESI†). Altogether, these results suggest that N incorporation leads to better electrical contact, lower electric impedance, and faster charge transfer kinetics for glycerol oxidation.

Product analysis

Glycerol oxidation products were collected and analyzed by ¹H and ¹³C nuclear magnetic resonance (NMR) spectroscopy (Fig. 2d, e). A relatively low potential of 1.35 V was chosen here to limit the

competitive OER. The ¹H NMR spectra before and after 12 hours of electrolysis identifies formic acid as the main product (Fig. 2d). Negligible changes in current density after 12 hours of electrolysis demonstrate the catalyst's high stability during extended operation (Fig. S9a, ESI†). LSV curves before and after 12 hours of electrolysis exhibit a slight deterioration in catalytic activity (Fig. S9b, ESI†). This may be attributed to a decrease in glycerol concentration and possible change in the electrolyte's pH.³² To further understand the stability of N-CoO_x, post 12-h LSV in a fresh electrolyte was compared to the LSV prior to electrolysis, where negligible changes in onset potential and overpotential are noticed (Fig. S10a, ESI†). Further, the intact Co 2p XPS spectrum after electrolysis confirm the superior stability of N-CoO_x toward oxidizing glycerol (Fig. S10b, ESI†). The products of glycerol electrolysis were further confirmed by the ¹³C NMR. As shown in Fig. S11, ESI†, formic acid remained as the main product identified after 60 hours of electrolysis, which correlates well with ¹H NMR findings. The small amount of carbonate detected in the ¹³C NMR spectra may be attributed to the high solubility of atmospheric CO₂ in strongly alkaline media. A decrease in glycerol concentration was also detected by ¹³C NMR, suggesting a successful electrically-driven glycerol conversion. In addition to formic acid, glyceric acid, glycolic acid, lactic acid, and acetic acid were detected at concentrations much lower than what was seen for formic acid (Fig. 2e). These intermediate species will be used to unravel the glycerol oxidation mechanism, which is discussed in the mechanism investigation section.

To determine the FE of formic acid, ¹H NMR peaks of formic acid at a range of standard concentrations were collected with respect to the formic acid calibration curve (Fig. S12a, b, ESI†). From this analysis, the FE for formic acid production at 1.35 V was calculated to be 96.2%, which exceeds most glycerol upgrading works reported (Table S2, ESI†).³²⁻³³ FEs at varied potentials were investigated in Figure 2f, where the FE reaches a maximum (96.2%) at 1.35 V and gradually decreases to 58% and 75% at 1.25 V and 1.5 V, respectively. The FE and potential dependence may be explained by the strength of C-C bonds, which are harder to break at lower potentials. Unfortunately, at higher potentials, OER competes with glycerol oxidation and diminishes glycerol conversion selectivity. N-CoO_x also demonstrated great durability and recyclability by maintaining an average FE of 93.8% after five cycles of electrolysis (Fig. 2g). Lastly, concentration changes of the reactant (glycerol), intermediate (glycolic acid), and the product (formic acid) were monitored during electrolysis (Fig. 2h). A linear relationship between the reaction time and the concentration of product generated (or reactant consumed) was observed, while the intermediate species demonstrated a nearly constant concentration throughout the reaction. Moreover, the FE of H₂ at cathode is found to be close to 100% in five successive electrolysis cycles (Fig. S13, ESI†). The result indicated that the HER is the only cathodic reaction, which also further indicates the replacing anodic OER with glycerol oxidation will not affect the cathodic half-reaction.

To determine the potential for N-CoO_x to oxidize other biomass-derived compounds, its catalytic activity towards ethylene glycol (EG) oxidation was investigated (Fig. S14a-c, ESI†). An onset potential of

1.25 V and a potential of 1.35 V at 10 mA cm⁻² were observed (1.0 M EG), which saved 0.23 V of the potential (10 mA cm⁻²) compared to OER (Fig. S12a, ESI[†]), thus proving EG oxidation with N-CoO_x reduces energy consumption at the anode. This potential shift was noticed at other current densities as well (10–40 mA cm⁻²) (Fig. S14b, ESI[†]). Regarding selectivity, an optimal FE of 62.3% at 1.40 V was obtained for formic acid production from EG (Fig. S14c, ESI[†]). From these results, we conclude that N-CoO_x exhibits promising results towards converting glycerol and ethylene glycol into value-added formic acid. Currently, commercial production of formic acid involves reacting methanol with toxic carbon monoxide at an elevated pressure. This reaction produces the intermediate species methyl formate, which is then transformed into formic acid by a two-step hydrolysis reaction (Fig. 1c). This approach involves intensive energy and cost inputs.¹⁷ Instead, our work provides a facile route to synthesize formic acid by biomass electrolysis at room-temperature and atmospheric pressure.

Mechanism investigation

The proposed reaction mechanism is provided in Fig. 3. In the first step, a primary hydroxyl group (-OH) on glycerol will be oxidized to an aldehyde via two-electron transfer.³⁴ Further, the aldehyde will be oxidized to a carboxyl group, forming glyceric acid, which is supported by the ¹H NMR (Fig. 2e). Then, we propose that the formic acid was produced with an oxidative cleavage of C-C bonds in glyceric acid and glycolic acid, where both intermediates are well identified by the NMR (Fig. 2e). Based on this route, one glycerol molecule may be completely converted into three formic acid molecules through an eight-electron transfer process. However, very small amounts of lactic acid and acetic acid are observed in the NMR results (Fig. 2e). Thus, we hypothesize that there is a minor reaction pathway (Fig. 3). In the minor reaction pathway, glyceraldehyde will reversibly react with OH⁻ to form dihydroxy acetone. Dihydroxy acetone is then converted into 2-hydroxypropenal/pyruvaldehyde after a

dehydration process. Further, 2-hydroxypropenal and pyruvaldehyde will convert to lactic acid after a Cannizzaro rearrangement. In the last step, the lactic acid will be oxidized to acetic acid and formic acid via C-C bond breakage.^{35–36} Similarly, the electrochemical oxidation mechanism for ethylene glycol conversion into formic acid is proposed in Fig. S15. In this mechanism, a primary -OH group from ethylene glycol is oxidized to an aldehyde via a two-electron process, followed by oxidized into carboxyl. Finally, the glycolic acid intermediate will completely convert into formic acid via an oxidative cleavage of C-C bonds.

Integrating glycerol electrooxidation with hydrogen generation

The results reported thus far are based on half-cell systems and demonstrate how well N-CoO_x facilitates the conversion of biomass-derived alcohols. Aside from its critical role in oxidizing biomass-derived alcohols, N-CoO_x also performs effectively as an HER catalyst under basic conditions. As displayed in Fig. S15a, ESI[†], N-CoO_x achieves an overpotential of 0.265 V at 10 mA cm⁻², whereas Co₃O₄ requires 0.423 V of overpotential to reach 10 mA cm⁻². Likewise, N-CoO_x's 147 mV dec⁻¹ Tafel slope implies N-CoO_x's fast kinetics towards HER (Fig. S16b, ESI[†]). To understand the catalyst's overall water splitting performance, N-CoO_x was simultaneously used as an anode and cathode for water electrolysis in a two-electrode system (Fig. S16a and 18a, ESI[†]). A high cell voltage close to 1.9 V was required to reach 10 mA cm⁻², which significantly contributes to OER's sluggish kinetics. Replacing OER with glycerol oxidation dramatically reduces the cell voltage to 1.59 V (10 mA cm⁻²) (Figure S17 and 18b, ESI[†]). O₂ gas evolution was not detected at the anode upon adding 1.0 M glycerol, indicating the catalyst's preference for glycerol oxidation over OER.

To further reduce the dependence on electricity and promote renewable energy utilization, a PEC cell equipped with a Pt-coated silicon nanowire (Si NW-Pt) photocathode was coupled with the N-

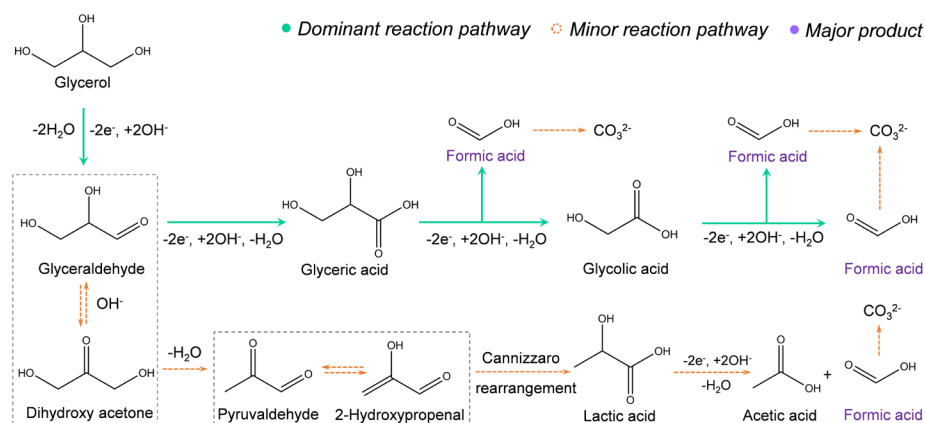


Fig. 3 Proposed reaction pathway of glycerol electro-oxidation on N-CoO_x. The solid green and dashed yellow arrows represent the major and minor reaction routes, respectively. Two-way dashed yellow arrows represent reversible processes. Formic acid was the major product (purple), while acetic acid and carbonate were minor products. Except for the unstable species that were difficult to detect under basic conditions (dashed rectangular boxes), NMR was employed to identify all intermediates and products and prove the feasibility of the proposed reaction routes. The route from glyceraldehyde to lactic acid is believed to undergo intermolecular dehydration and rearrangement under basic conditions, which does not involve electron transfer. All other routes involve electrochemical oxidation processes with related electron transfer pathways.

ARTICLE

CoO_x anode. The schematic diagram in Fig. 4a and digital photos in Fig. 4b and Fig. S22, ESI[†] for the hybrid system displays how the Si NW-Pt photocathode may drive glycerol oxidation and HER simultaneously under 1 sun illumination with a limited external bias. In this work, we utilized our previously reported method to fabricate Si NW-Pt photocathodes.³⁷ SEM images and corresponding EDX elemental mapping of the Si NW-Pt photocathode are demonstrated in Fig. S18 and Fig. S20, ESI[†], where the silicon nanowires are ~2 μm long and Pt nanoparticles are uniformly presented across the surface of the silicon nanowires. Upon evaluating the HER performance of the Si NW-Pt photocathode under both basic (1.0 M KOH) and acidic (0.5 M H₂SO₄) conditions, the photocathode showed an onset potential of 0.25 V vs. RHE in both electrolytes (Fig. S21, ESI[†]). Si NW-Pt was then coupled with N-CoO_x anode (N-CoO_x | Si NW-Pt) into a two-electrode system for simultaneous glycerol oxidation and PEC hydrogen evolution. As shown in Fig. 4c, before adding glycerol, the N-CoO_x | Si NW-Pt hybrid system required a cell voltage of 1.34 V to reach 10 mA cm⁻², which is much lower than the energy required in N-CoO_x | N-CoO_x system (1.81 V, no glycerol). This voltage was further reduced to 1.15 V after adding 1.0 M glycerol, much lower than that of N-CoO_x | N-CoO_x system (1.59 V, with glycerol). To the best of our knowledge, it is the first time that PEC hydrogen evolution has been coupled with glycerol oxidation, which demonstrates great success in saving the overall cell voltage (Fig. 4d, Table S2, ESI[†]). The cell voltage that reported here is at least ~0.2 V less comparing with

conventional water splitting configurations, reducing ~30% electricity consumption.

Conclusion

In summary, we demonstrated an inexpensive N-CoO_x electrocatalyst that could efficiently oxidize glycerol (a cheap byproduct of biodiesel production) and biomass-derived ethylene glycol. N-CoO_x successfully converts glycerol into high-value formic acid at a low potential of 1.31 V (10 mA cm⁻²), which is 0.27 V less than the potential required to drive OER. Additionally, selective conversion of glycerol to formic acid achieved FEs up to 96.2%. The catalyst also exhibited a high activity for oxidizing ethylene glycol (1.35 V at 10 mA cm⁻²) to formic acid with 62.3% FE. Coupling N-CoO_x anode with a Si NW-Pt photocathode in a two-electrode PEC cell further reduced the cell voltage (only need 1.15 V to produce 10 mA cm⁻²) required to concurrently upgrade glycerol to formic acid and generate hydrogen fuel. These remarkable results revealed that glycerol electrooxidation would be a promising alternative to traditional energy extensive OER process due to low electricity consumption. Besides, harvesting solar energy further reduced the system's dependence on electricity. More importantly, utilizing glycerol electrooxidation to replace OER will generate significant economic profits relative to typical water electrolysis. As a consequence, solar-assisted co-electrolysis of water and high-volume chemicals may be an attractive pathway to achieving sustainable co-production of hydrogen energy and high-value chemicals due to improved techno-economics. This work provides a solid foundation to design devices for concurrent fuel generation and biomass upgradation in the future.

Experimental

Materials

Bis (N, N'-di-i-propylacetamidinato) cobalt (II) (C₁₆H₃₄CoN₄, 99.99%) was purchased from STREM. Cobalt (II) nitrate hexahydrate (Co(NO₃)₂·6H₂O, 98%), and gallium indium alloy were purchased from Alfa Aesar. Ammonium chloride (NH₄Cl, 99%), potassium hexachloroplatinate (IV) (K₂PtCl₆, 98%), glycerol (C₃H₈O₃, 99%), formic acid (CH₂O₂, 98%), ethylene glycol (C₂H₆O₂, 99%), and deuterium oxide (D₂O, 99.9%) were purchased from Sigma-Aldrich. Glycolic acid (C₂H₄O₃, 98%, TCI) and glyceric acid (C₃H₆O₄, 98%) were purchased from TCI. Silicon wafer (p-type, boron doping) was obtained from WAFERPRO. Silver paste was from Ted Pella Inc. Copper wire was purchased from Fisher Scientific. Toray Carbon fiber paper (TGP-H-60) was obtained from Advance Instruments. Deionized water (DIW) was used in all experiments. All chemicals and materials were directly used without further purifications and treatments.

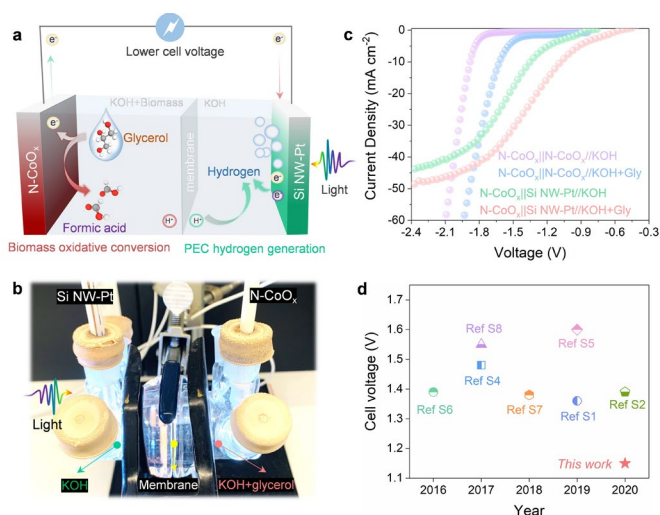


Fig. 4 The N-CoO_x | Si NW-Pt hybrid system. **a** Schematic diagram and **b** Digital photo of the N-CoO_x | Si NW-Pt hybrid system. **c** Cathodic current-voltage curves of the hybrid photoelectrochemical system. **d** A comparison of cell voltages in recently reported hybrid systems. Overall, our strategy has the potential to save at least 0.4 V in cell voltage compared to the

Synthetic procedures

The N-CoO_x were deposited by GEM Star XT Atomic Layer Deposition System. In a typical process, a nitrogen-containing cobalt-based molecular compound (Bis (N, N'-di-i-propylacetamidinato) cobalt (III)) was used as the cobalt and nitrogen precursor. Ozone and helium were employed as the oxidizer and carrier gas, respectively. The Cobalt precursor was heated to 85 °C and the manifold was maintained at 115 °C to avoid condensation of the precursors in the gas lines. The temperature in deposition chamber was 150 °C. Nitrogen doped CoO_x (N-CoO_x) was uniformly deposited on carbon fiber paper after 300 ALD cycles.

Co₃O₄ nanosheets on carbon fiber paper was fabricated by electrodeposition method. Typically, α-Co(OH)₂ was first electrodeposited on carbon fiber paper in 100 ml of 0.02 M Co(NO₃)₂·6H₂O solution with 0.1 M NH₄Cl at -2.0 mA for 10 min. Then, Co₃O₄ was obtained by annealing α-Co (OH)₂ nanosheet in air under 250 °C for 2 h. All electrodeposition experiments were conducted via a two-electrode system where carbon fiber paper and graphite rod were used as work and counter electrode, respectively.

Si NW-Pt photoelectrode fabrication: A metal-assisted chemical etching strategy was employed to synthesize silicon nanowires (Si NW). Typically, back side of silicon wafer was firstly covered by polyimide to avoid being etched, which was then sonicated in acetone and DI water for 15 min to remove impurities. Further, the wafer was soaked in 5% HF for 90 s to etch silicon oxide layer. Then, the clean-washed wafer was soaked in 10% HF solution with 0.02 M AgNO₃ for 60 s to deposit silver particles on surface. Subsequently, the wafer was soaked into a mixture of 10% HF and 30% H₂O₂ (10:1, vol%) for 10 min and then into 35% HNO₃ for 15 min to remove Ag residual. Finally, the wafer was used to fabricate photoelectrode according to following steps: 1) silicon backside was cleaned by 5 wt% HF for 30 s; 2) ohmic contact was formed by coating Ga-In eutectic on the backside; 3) the backside was fixed on a conductive copper coil with conductive silver paint; 4) the copper coil tail was passed through a glass tube for electric contact. 5) the photoelectrode assembly was encapsulated by coating Loctite 9462 epoxy and dried at room temperature overnight. For platinum deposition, the obtained photoelectrode was firstly cleaned in 5 wt% HF for 30 s and then soaked into 1 wt% HF solution with 5 mM K₂PtCl₆ for 60 s.

Material characterizations:

X-ray diffraction (XRD) pattern was collected on PANalytical X' Pert with Cu-Kα radiation (λ = 1.5418 Å). X-ray photoelectron spectroscopy (XPS) measurements were performed using the Kratos AXIS Supra equipped with a monochromatic Al Kα X-ray source, running at a power of 300W, and operating at 15 kV. All samples were measured with a 300 x 700 μm² spot size and operating chamber pressure < 10⁻⁸ torr. XPS spectra were fitted with XPS peak software to analyse the atomic compositions and the possible chemical species. The binding energy scale was calibrated using the C 1s peak at 284.8 eV. Electron paramagnetic resonance (EPR) measurements were performed on Magnostech MS 5000. Scanning transmission electron microscopy (STEM) was performed using the JEOL Grand and high-angle angular dark-filled (HAADF)-STEM images

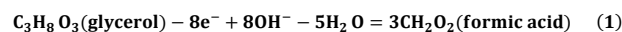
were acquired by a convergence semiangle of 22 mrad and inner and outer collection angles of 83 and 165 mrad, respectively. Energy dispersive X-ray spectroscopy (EDS) was conducted using JEOL dual EDS detectors and a specific high count analytical TEM holder. For TEM sample preparation, the copper TEM grid was directly put into ALD for N-CoO_x deposition.

Photo-/Electro-chemical measurements

All electrochemical measurements were carried on CHI 600E and 660E workstations. We initially evaluated the performance of our samples for HER, OER, glycerol oxidation, and ethylene glycol oxidation in a typical three-electrode system where graphite rod and Ag/AgCl were used as counter and reference electrode, respectively. Then the N-CoO_x anode and Si NW-Pt photocathode were coupled in a two-electrode system to investigate hybrid glycerol electrolysis and hydrogen evolution. A nafion film was used to separate the oxidation and reduction reactions. A steady DC-powered 150 W Xe-arc lamp (Newport) was used as a simulated sunlight source. A water filter was used to block the infrared irradiation. The incident light intensity was calibrated to 100 mW cm⁻² (one sun) using a Si photodiode. All LSV curves were collected in a scan rate of 5 mVs⁻¹ and without IR compensation. All the electrochemical measurements were performed in N₂-saturated electrolyte. The potentials were calibrated to reverse hydrogen electrode (RHE) according to the equation: E_{RHE} = E_{Ag/AgCl} + 0.059 pH + 0.197 V.

Product quantification

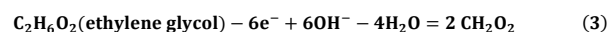
A long-term electrolysis experiment was employed to determine products of glycerol oxidation and ethylene glycol oxidation. Electrolytes after electrolysis were collected and analysed by nuclear magnetic resonance (NMR) spectrometer. All liquids to be tested contained 540 μl electrolyte and 60 μl D₂O and were measured by ¹H and ¹³C NMR spectra. ¹H NMR and ¹³C NMR spectra were recorded on Varian spectrometers at 400 MHz. Formic acid standard was prepared by dissolving formic acid (15 mM for ¹H NMR and 60 mM for ¹³C NMR) in 1.0 M KOH aqueous solution, and ¹H and ¹³C NMR spectra of the standard were collected under same conditions as the solution after biomass-polyol electrolysis. The gaseous products produced from cathode after electrolysis was collected and analysed by gas chromatography (GC-2014C, SHIMADZU). According to the proposed reaction pathway, the conversion from glycerol to formic acid could be described by following equation (1).



Hence, the Faradaic efficiency of formic acid for glycerol oxidation can be determined by equation (2),

$$\text{FE}(\%) = \frac{N(\text{formic acid yield})}{Q_{\text{total}}/(Z_1 \times F)} \times 100\% \quad (2)$$

and the conversion from glycerol to formic acid could be described by following equation (3).



Similarly, the Faradaic efficiency of formic acid for ethylene glycol oxidation was described by equation (4),

$$\text{FE}(\%) = \frac{N(\text{formic acid yield})}{Q_{\text{total}}/(Z_2 \times F)} \times 100\% \quad (4)$$

in which Q_{total} is the total charge passed through the electrodes, $Z_1=8/3$ and $Z_2=3$ are the numbers of electrons that form a mole of formic acid, and F is the Faraday constant ($96,485 \text{ C mol}^{-1}$).

Author contributions

J. G. and X. X. lead the project. Z. K. designed and performed experiments. W. N. assisted with product analysis by NMR. X. Y. and X. P. conducted the STEM characterizations. D. H. and X. S. helped with mechanism studies for this research. S.Y. helped with some electrochemical measurements and involved into writing this paper.

Conflicts of interest

The authors declare no competing interests.

Acknowledgements

Jing Gu acknowledges San Diego State University (SDSU) start-up funds and NSF award (CEBT-1704992) to support this research. We gratefully acknowledge the UC Irvine Materials Research Institute (IMRI) for helping with STEM and XPS characterizations. IMRI was funded in part by the National Science Foundation Major Research Instrumentation Program under grant no. CHE-1338173.

References

- M. S. Dresselhaus and I. L. Thomas, *Nature*, 2001, **414**, 332-337.
- J. A. Turner, *Science*, 2004, **305**, 972-974.
- A. Landman, H. Dotan, G. E. Shter, M. Wullenkord, A. Houaijia, A. Maljusch, G. S. Grader and A. Rothschild, *Nat. Mater.*, 2017, **16**, 646-651.
- M. F. Lagadec and A. Grimaud, *Nat. Mater.*, 2020, **19**, 1140-1150.
- Hydrogen Production Cost, <https://www.sciencedirect.com/topics/engineering/hydrogen-production-cost>, accessed.
- N. v. Hulst, The clean hydrogen future has already begun, <https://www.iea.org/commentaries/the-clean-hydrogen-future-has-already-begun>, accessed.
- I. Roger, M. A. Shipman and M. D. Symes, *Nat. Rev. Chem.*, 2017, **1**, 1-13
- J. Wang, W. Cui, Q. Liu, Z. Xing, A. M. Asiri and X. Sun, *Adv. Mater.*, 2016, **28**, 215-230.
- W. Wang, Y. B. Zhu, Q. Wen, Y. Wang, J. Xia, C. Li, M. W. Chen, Y. Liu, H. Li, H. A. Wu and T. Zhai, *Adv. Mater.*, 2019, **31**, e1900528.
- B. Zhu, Z. Liang and R. Zou, *Small*, 2020, **16**, e1906133.
- Y. Liu, J. Zhang, Y. Li, Q. Qian, Z. Li, Y. Zhu and G. Zhang, *Nat. Commun.*, 2020, **11**, 1853.
- S. Verma, S. Lu and P. J. A. Kenis, *Nat. Energy*, 2019, **4**, 466-474.
- R. Ciriminna, C. D. Pina, M. Rossi and M. Pagliaro, *Eur. J. Lipid Sci. Tech.*, 2014, **116**, 1432-1439.
- N. Han, Y. Wang, H. Yang, J. Deng, J. Wu, Y. Li and Y. Li, *Nat. Commun.*, 2018, **9**, 1320.
- A. A. N. Afshar, CHEMICAL PROFILE: FORMIC ACID http://chemplan.biz/chemplan_demo/sample_reports/Formic_Acid_Profile.pdf, accessed.
- Formic Acid Prices, <https://www.intratec.us/chemical-markets/formic-acid-price>, accessed.
- D. A. Bulushev and J. R. H. Ross, *ChemSusChem*, 2018, **11**, 821-836.
- Z. Zhang, L. Xin and W. Li, *Appl. Catal. B: Environ.*, 2012, **119-120**, 40-48.
- J. Qi, L. Xin, D. J. Chadderton, Y. Qiu, Y. Jiang, N. Benipal, C. Liang and W. Li, *Appl. Catal. B: Environ.*, 2014, **154-155**, 360-368.
- M. Simões, S. Baranton and C. Coutanceau, *Appl. Catal. B: Environ.*, 2010, **93**, 354-362.
- H. J. Kim, S. M. Choi, M. H. Seo, S. Green, G. W. Huber and W. B. Kim, *Electrochem. Commun.*, 2011, **13**, 890-893.
- S. Lee, H. J. Kim, E. J. Lim, Y. Kim, Y. Noh, G. W. Huber and W. B. Kim, *Green Chem.*, 2016, **18**, 2877-2887.
- A. Zalineeva, A. Serov, M. Padilla, U. Martinez, K. Artyushkova, S. Baranton, C. Coutanceau and P. B. Atanassov, *J. Am. Chem. Soc.*, 2014, **136**, 3937-3945.
- M. Simoes, S. Baranton and C. Coutanceau, *ChemSusChem*, 2012, **5**, 2106-2124.
- S. Wang, Y. Wang, S. L. Zhang, S. Q. Zang and X. W. D. Lou, *Adv. Mater.*, 2019, **31**, e1903404.
- Q. Yu, C. Liu, X. Li, C. Wang, X. Wang, H. Cao, M. Zhao, G. Wu, W. Su, T. Ma, J. Zhang, H. Bao, J. Wang, B. Ding, M. He, Y. Yamauchi and X. S. Zhao, *Appl. Catal. B: Environ.*, 2020, **269**, 118757.
- Z. Wang, W. Xu, X. Chen, Y. Peng, Y. Song, C. Lv, H. Liu, J. Sun, D. Yuan, X. Li, X. Guo, D. Yang and L. Zhang, *Adv. Funct. Mater.*, 2019, **29**, 1902875.

28. D. He, X. Song, W. Li, C. Tang, J. Liu, Z. Ke, C. Jiang and X. Xiao, *Angew. Chem. Int. Ed.*, 2020, **59**, 6929-6935.
29. M. Yu, Z. Wang, C. Hou, Z. Wang, C. Liang, C. Zhao, Y. Tong, X. Lu and S. Yang, *Adv. Mater.*, 2017, **29**, 1602868.
30. Z. Chen, Y. Song, J. Cai, X. Zheng, D. Han, Y. Wu, Y. Zang, S. Niu, Y. Liu, J. Zhu, X. Liu and G. Wang, *Angew. Chem. Int. Ed.*, 2018, **57**, 5076-5080.
31. C. Yin, Y. Liu, Q. Xia, S. Kang, X. Li, Y. Wang and L. Cui, *J. Colloid Interface Sci.*, 2019, **553**, 427-435.
32. Y. Li, X. Wei, L. Chen, J. Shi and M. He, *Nat. Commun.*, 2019, **10**, 5335.
33. X. Han, H. Sheng, C. Yu, T. W. Walker, G. W. Huber, J. Qiu and S. Jin, *ACS Catal.*, 2020, **10**, 6741-6752.
34. M. H. Haider, N. F. Dummer, D. W. Knight, R. L. Jenkins, M. Howard, J. Moulijn, S. H. Taylor and G. J. Hutchings, *Nat. Chem.*, 2015, **7**, 1028-1032.
35. C. Dai, L. Sun, H. Liao, B. Khezri, R. D. Webster, A. C. Fisher and Z. J. Xu, *J. Catal.*, 2017, **356**, 14-21.
36. M. Pagliaro, R. Ciriminna, H. Kimura, M. Rossi and C. Della Pina, *Angew. Chem. Int. Ed.*, 2007, **46**, 4434-4440.
37. F. Yang, J. A. Aguiar, M. Fairchild, W. Vakki, S. Younan, Y. Zhou, L. Zhuo and J. Gu, *Adv. Mater. Interfaces*, 2019, **6**, 1802085.